

Ptpn20 Deletion in H-tx Rats Facilitates Cotransporter-mediated Water Transport in the Choroid Plexus: Evidence of Genetic Risk for Hydrocephalus in an Experimental Study

Hanbing Xu

Juntendo University Graduate School of Medicine

Masakazu Miyajima (✉ mmasaka@juntendo.ac.jp)

Juntendo Tokyo Koto Geriatric Medical Center

Madoka Nakajima

Juntendo University Graduate School of Medicine

Ikuko Ogino

Juntendo University Graduate School of Medicine

Kaito Kawamura

Juntendo University Graduate School of Medicine

Chihiro Akiba

Juntendo Tokyo Koto Geriatric Medical Center

Chihiro Kamohara

Juntendo University Graduate School of Medicine

Koichiro Sakamoto

Juntendo University Graduate School of Medicine

Kostadin Karagiozov

Juntendo University Graduate School of Medicine

Eri Nakamura

Juntendo University Graduate School of Medicine

Nobuhiro Tada

Juntendo University Graduate School of Medicine

Hajime Arai

Juntendo University Graduate School of Medicine

Akihide Kondo

Juntendo University Graduate School of Medicine

Keywords: cerebrospinal fluid, choroid plexus, H-Tx rats, hydrocephalus, NKCC1 cotransporter

Posted Date: February 2nd, 2022

DOI: <https://doi.org/10.21203/rs.3.rs-1305224/v1>

License:  This work is licensed under a Creative Commons Attribution 4.0 International License.

[Read Full License](#)

Abstract

Background

Congenital hydrocephalus occurs with some inheritable characteristics, but the mechanisms of its development remain poorly understood. Animal models provide the opportunity to identify potential genetic causes in this condition. The Hydrocephalus-Texas (H-Tx) rat strain is one of the most studied animal models for investigating the causative genetic alterations and analyzing downstream pathogenetic mechanisms of congenital hydrocephalus.

Methods

Comparative genomic hybridization (CGH) array on non-hydrocephalic and hydrocephalic H-Tx rats was used to identify causative genes of hydrocephalus. Targeted gene knockout mice were generated by CRISPR/Cas9 to study the role of this gene in hydrocephalus.

Results

CGH array revealed a copy number loss in chromosome 16p16 region in hydrocephalic H-Tx rats, encompassing the *Ptpn20* gene, without change in most non-hydrocephalic H-Tx rats. *Ptpn20*-knockout (*Ptpn20*^{-/-}) mice were generated and found to develop ventriculomegaly. Furthermore, high expression of phosphorylated Na-K-Cl cotransporter 1 (pNKCC1) was identified in the choroid plexus (CP) epithelium of mice lacking *Ptpn20*.

Conclusions

The high level of pNKCC1 in CP epithelium may cause the overproduction of cerebrospinal fluid and contribute to the formation of hydrocephalus in *Ptpn20*^{-/-} mice. *Ptpn20* may be a potential therapeutic target in the treatment of hydrocephalus.

Introduction

Hydrocephalus represents excess accumulation of cerebrospinal fluid (CSF) in the cerebral ventricles and subarachnoid space. In humans, congenital hydrocephalus occurs with a high frequency of 0.5–1.5 per 1000 births, representing the most common neurological disorder requiring surgery in children [1-3]. Despite the high prevalence of congenital hydrocephalus, knowledge about the pathophysiological mechanisms leading to this disorder remains extremely limited. A large body of evidence suggests that congenital hydrocephalus is an inheritable disorder and characterization at the molecular level should greatly increase the understanding of the disease and lead to new therapies. However, relatively few genes in humans have been linked with hydrocephalus to date, including *L1CAM*, *MPDZ*, and *CCDC88C* [4-6]. Less than 5% of mutations in these genes account for primary congenital hydrocephalus cases [7]. As animal models of inherited disease provide opportunities to identify potential genetic causes of disease in humans, a variety of genes causing hydrocephalus in rodents have been identified and

characterized over the past decades in transgenic animal models, including the Hydrocephalic-Texas (H-Tx) rat, the Wistar-Lewis rats, the hydrocephalus-1 mouse, the hydrocephalus with hop gait mouse, and the TGF-beta1 mouse [8-14].

Among these, the H-Tx rat strain, first described in 1981, is widely used as a model of congenital hydrocephalus resulting from a spontaneous mutation to study the pathogenesis of the disease [15]. Hydrocephalus in H-Tx rats develops in early gestation via a complex mode of inheritance and with a prevalence of 30–50% [16]. Ventricular dilatation starts to occur from days 17–18 of gestation and is associated with aqueductal stenosis [17, 18]. Pups with severe hydrocephalus are detected at birth by a domed head and die at 4–6 weeks of age. Breeding data from crosses between H-Tx rats and Sprague-Dawley (SD) rats have indicated that hydrocephalus in H-Tx rats is a single autosomal recessive gene disease [19], but a series of studies by Jones *et al* indicated that the phenotypic expression of congenital hydrocephalus in H-Tx rats is controlled by a combination of genetic and epigenetic factors [16, 20-24].

The genetic abnormality causing congenital hydrocephalus in H-Tx rats remains only partially understood. In this study, we performed copy number analysis to investigate candidate genes potentially responsible for hydrocephalus in H-Tx rats. Under this approach, we identified a copy number loss in the *Ptpn20* gene in hydrocephalic H-Tx rats and generated *Ptpn20*-knockout mice, then tested for genotypic and phenotypic differences from wild-type (WT) mice. Based on our findings, we propose a pathophysiological mechanism to explain the formation of hydrocephalus and a possible therapeutic target for its treatment.

Materials And Methods

Animals

All experimental animals were group-housed with 2–5 animals per cage and maintained in a temperature- and humidity-controlled facility ($23 \pm 1^\circ\text{C}$, $55 \pm 5\%$ humidity) on a 12-h light/dark cycle at our animal care facility in the Center for Experimental Medicine of Juntendo University, Japan. All procedures involving animals were approved by the Ethics Review Committee for Animal Experimentation of the Juntendo University School of Medicine (rats: approval no. 288; mice: approval no. 1337) and followed the Principles of Laboratory Animal Care as outlined by the National Institutes of Health.

Study animals used in genetic identification included hydrocephalic H-Tx (H-Tx (+)) rats and non-hydrocephalic H-Tx (H-Tx (-)) rats at 18 days gestation (E18), 1 day postnatal (P1) and 1 week postnatal (P7), and Wistar and SD rats at P1. Among these, E18 H-Tx (+) and H-Tx (-) rats were determined from the size of the ventricles on tissue sections. P1 H-Tx (+) and H-Tx (-) rats were determined by the characteristic “domed head” appearance on gross examination (Additional file 1: Fig. S1A, B). H-Tx (-), Wistar and SD rats served as controls.

Animals were decapitated for dissection of the brain after induction of deep anesthesia using intraperitoneal pentobarbital (50 mg/kg body weight). Each brain sample was immediately stored in

RNA/*later*[®] solution (AM7021; Thermo Fisher Scientific, Waltham, MA, USA) for DNA, RNA and protein extractions.

Identification of genetic risk in H-Tx rats

Comparative genomic hybridization array

DNA was extracted from the brain of H-Tx (+) rats and H-Tx (-) rats at E18, and genome-wide DNA copy number analysis was performed using a SurePrint G3 Rat Comparative genomic hybridization array (CGH) Microarray kit 1x1M SG13464375 (ID-027065; Agilent Technologies, Santa Clara, CA, USA) according to the protocol from the manufacturer. Data were extracted using Feature Extraction version 10.1.1.1 software (Agilent Technologies), and analyses were performed using Agilent Genomic Workbench Standard Edition version 5.0.14 software (Statistical algorithm ADM-2, threshold of 6.0, fuzzy zero correction). Non-redundant copy number abnormalities were called as a minimum of three consecutive probes and log₂ ratio > 0.3 for gains and < -0.3 for losses were considered significant.

Real-time PCR of copy number

Copy number quantification was performed by TaqMan[®] quantitative polymerase chain reaction on the brain tissues of E18 H-Tx (+) and H-Tx (-) rats using an ABI7500 real-time PCR system (Applied Biosystems, Thermo Fisher Scientific). TaqMan Copy Number assays (*Ptpn20* exon 6-7, Custom ID: CC70L9K, CCLJ15L) were run simultaneously with TaqMan Copy Number Reference assays (*Rnase11* (Rn02349567_s1), *Ftmt* (Rn01492073_s1) and *Hus1* (Rn02115575_s1)) (Applied Biosystems) according to the instructions from the manufacturers. Copy number variations were analyzed using ABI7500 software (Applied Biosystems) and Copy Caller version 2.0 software (Applied Biosystems).

Real-time PCR of *Ptpn20* mRNA

Total RNA (500 ng) was converted into single-stranded cDNA using SuperScript™ IV VILO™ (SSIV VILO) Master Mix (Invitrogen, Thermo Fisher Scientific). The ABI 7500 Real-time PCR System (Applied Biosystems) and TaqMan[®] Gene Expression Assays (Applied Biosystems) were used according to the instructions from the manufacturer to quantify gene expression. Assay IDs are listed in additional file 5: Table S2.

Expressions of target genes were standardized to the expression of *Actb*. The presence of a single PCR amplicon was confirmed by melting curve analysis. Expressions of each gene in each sample were analyzed in triplicate.

Protein expression of *Ptpn20*

Proteins were extracted from CP (Additional file 6: Table S3) and lysed in 50 ml of lysis buffer (N-PER; Thermo Fischer Scientific) containing protease inhibitor cocktail (cOmplete ULTRA Mini EDTA-free EASYpack; Roche, Basel, Switzerland). Lysates were clarified by centrifugation at 20,000 g at 4°C for 10

min, and protein concentrations of the resultant supernatants were determined using BCA Protein Assay Kits (Thermo Fischer Scientific). After 10–15 µg of proteins was heated at 70°C for 10 min in NuPAGE® LDS Sample Buffer (NP0008; Invitrogen) and NuPAGE® Sample Reducing Agent (NP0009; Invitrogen), samples were electrophoresed on 4–12% NuPAGE® Bis-Tris Mini Gel by NuPAGE® MOPS SDS Running Buffer (20') (NP0001; Invitrogen) Running Buffer (20'), then transferred to a polyvinylidene fluoride membrane. Primary antibodies are listed in additional file 6: Table S3. Signals were detected by chemiluminescence using a WesternBreeze kit (WB7103; Invitrogen). Immunoreactive bands were detected using ImageLab version 4.1 software (Bio-Rad Laboratories, Hercules, CA, USA).

Immunofluorescence of the CP

Animal brains were removed and postfixed with 4% paraformaldehyde in 0.01-M phosphate buffer (pH 7.2). Paraffin-embedded sections (4 µm) and cryosections (30 µm) were blocked with 5× SEA BLOCK™ blocking buffer (37527; Thermo Fisher Scientific) and 1% donkey serum in Phosphate buffered saline (PBS; AJ9P003; TaKaRa, Shiga, Japan) for 30 min, incubated in primary antibody overnight at 4°C and secondary antibodies for 60 min at room temperature. Vibratome sections (300 µm) were blocked using the same blocking buffer with 0.05% TritonX and 1% donkey serum in PBS for 30 min, then incubated in primary antibody for 2 days at 4°C and secondary antibodies for 2-h at room temperature. Primary and secondary antibodies are listed in additional file 7: Table S4. Nuclei in all sections were counterstained with ProLong Gold and SlowFade Gold Antifade Reagent with DAPI (4',6-diamidino-2-phenylindole; P36935; Molecular Probes®, Invitrogen). Images were acquired with a confocal scanning microscope (TCS-SP5; Leica Microsystems, Wetzlar, Germany). Leica Application Suite Advanced Fluorescence Lite (Leica Microsystems) was used for image acquisition and processing.

Expression and role of *Ptpn20* in mice

Immunohistochemistry

Brain and six other tissues (testis, kidney, heart, pancreas, liver and spleen) of 4-week-old C57BL/6J mice were fixed in 4% paraformaldehyde fixative (33111; Muto Pure Chemicals Co., Tokyo, Japan) for at least 1 week, embedded in paraffin, and cut into 6-µm sections. Endogenous peroxidase was blocked by incubation of brain sections with 0.3% hydrogen peroxide for 30 min. Sections were blocked with 5× SEA BLOCK Blocking Buffer and 1% donkey serum in PBS at 25°C for 30 min. Sections were incubated with rabbit PTPN20A antibody (CSB-PA199334, 1:50 dilution; CUSABIO, Houston, TX, USA) overnight at 4°C. The following day, sections were incubated with EnVision™ System Labeled Polymer (DAKO, Glostrup, Denmark) as the secondary antibody for 30 min at room temperature. Finally, sections were stained with 3,3'-diaminobenzidine and counterstained with Mayer's hematoxylin, dehydrated, cleared, and mounted. Sections were viewed under an E800 microscope (Nikon, Tokyo, Japan) and images were captured with an AxioCam 506 color digital camera using AxioVison Rel version 4.7.2.0 image-processing software (Carl Zeiss Microimaging GmbH, Jena, Germany).

Generation of *Ptpn20* knockout mice

Knockout mouse lines were generated using a CRISPR/Cas9 system in C57BL/6J mice with the single guide RNA (sgRNA) sequence (exon 4; CCTGAATCTCCGCAACTCTTGC, underlined is the protospacer adjacent motif sequence from GRCm38.p6).

Both sgRNA and Cas9 protein were injected into the cytoplasm of fertilized one-cell eggs using continuous pneumatic pressure. Eggs were cultured in modified Whitten's medium for approximately 24 h and developed to 2-cell stage embryos. Two-cell stage embryos were transferred into each oviduct of pseudopregnant Institute of Cancer Research (ICR) recipient females that had been mated to vasectomized ICR male mice. Embryo transfer to pseudopregnant females was performed on the day the vaginal plug was detected. After birth, genomic DNA was extracted from tail tips of mutant F0 mice and subjected to PCR using primers. The band was evaluated for amounts of mismatch-digestion fragments. To verify the genotype of mice, PCR amplification was performed using AmpliTaqGold®360Mastert Mix (catalog no. 4398881; Thermo Fischer Scientific) from mouse DNA for sequencing. PCR primers were as follows: forward, 5'-ATA GAA CAG TCT AGC CGT AAC TCA C-3'; reverse, 5'-TTC CCA TCT TGG CTG CAT CAC-3'.

Genome DNA was extracted from mouse tails using a DNeasy Blood & Tissue Kit (Cat. no. 69506; Qiagen, Hilden, Germany). The primer sequence used to amplify exon 4 sequences by AmpliTaq Gold™360Master Mix (no. 4398881; Thermo Fisher Scientific) was designed as follows: forward, 5'-TCA TGG ACA CTG AAA TAC AGG-3'; reverse, 5'-CTC TTA GAC CAT TGA CGC TAT T-3'.

Cycling conditions consisted of an initial 12-min denaturation step at 95°C followed by 35 cycles of 95°C for 30 s, annealing at 60°C for 30 s and extension at 72°C for 30 s, then final extension at 72°C for 7 min.

PCR products were sequenced on an ABI 3500 Genetic Analyzer using the BigDye Terminator Cycles Sequencing Kit v3.1 (Thermo Fisher Scientific). Samples were analyzed using Seq Scanner version 2 (Thermo Fisher Scientific) and compared with the public sequence in GenBank (NC_000080.6: *Ptpn20*).

Transmission electron microscopy of *Ptpn20*-knockout mice

Fresh brains from 8-week-old WT and *Ptpn20*^{-/-} mice were perfused with 4% paraformaldehyde. Materials were immersed in 2.5% glutaraldehyde solution after being cut into smaller fragments for TEM (1'2 mm²). Samples were washed with PBS, post-fixed in 2% osmium tetroxide for 2-h at 4°C and dehydrated in graded concentrations of ethanol. For TEM, samples were placed in resin for 4 days at 60°C. Ultrathin sections were observed under an HT7700 electron microscope (Hitachi High-Technologies, Tokyo, Japan).

Measurement of the lateral ventricle

Fresh brains 8-week-old WT and *Ptpn20*^{-/-} mice were postfixed in 4% paraformaldehyde for 72-h, equilibrated in 30% sucrose solution for 24-h at 4°C, then embedded in embedding matrix and frozen at

-80°C for further use. Coronal sections of 30 µm were obtained using a freezing microtome and stained with HE according to standard methods. We viewed and photographed sections using the E800 microscope, and images were captured with an AxioCam 506 color Digital Camera using AxioVison Rel version 4.7.2.0 image-processing software.

Widths of the brain and lateral ventricles were measured on sections at 0.5 cm anterior to the bregma. The ratio of ventricular width to brain width (VBR) was used to determine the degree of ventricular dilatation.[22] Data were calculated as mean ± standard deviation for WT. Differences between WT and *Ptpn20*^{-/-} mice were evaluated using the Mann-Whitney *U* test.

Ventricular injection of dye

Eight-week-old WT and *Ptpn20*^{-/-} mice were deeply anesthetized by pentobarbital sodium (100 mg/kg; Kyoritsu Seiyaku, Tokyo, Japan). The head was fixed into a stereotaxic apparatus (Narishige Scientific Instrument Laboratory, Tokyo, Japan), and a small burr hole was drilled in the cranium on the right, 1 mm lateral to the bregma. The needle of a microsyringe (MS-10; Ito Corporation, Shizuoka, Japan) was slowly inserted into the lateral ventricle 4 mm from the brain surface through the hole and Evans blue dye (6 µl; FUJIFILM, Wako Pure Chemical Corporation, Osaka, Japan) was injected at 2 µl/min. Ten minutes after injection, mouse brains were harvested, fixed in 4% paraformaldehyde for 72-h, then cut into 1-mm-thick coronal slices.

Real-time PCR, immunoblot and immunofluorescence

These three methods are similar to those used in the first part, but the results in the second part of the real-time PCR were quantified using the $2^{-\Delta\Delta Ct}$ method. Reagents are listed in additional file 5-7: Tables S2–4.

Statistical analysis

All experimental results are presented as mean ± standard deviation. Real-time PCR was performed as at least five independent experiments. Significant differences among groups were determined using Student's *t*-test. Statistical differences of the lateral ventricle between WT and *Ptpn20*^{-/-} mice were assessed by the Mann-Whitney *U* test. Results were considered statistically significant for values of $P < 0.05$.

Results

Identification of causative gene for hydrocephalus in H-Tx rats

The SurePrint G3 Rat Genome CGH Microarray kit was used to compare the copy numbers of genes in the brains of non-hydrocephalic H-Tx (H-Tx (-)) rats and hydrocephalic H-Tx (H-Tx (+)) rats. Among 30,584 genes tested, we found 47 genes with copy number variations in the brains. Although we did not detect any copy number variations that were present in all H-Tx (+) rats and not in H-Tx (-) rats among these 47

genes, a 14-kbp loss from chromosome region 16p16 was found in all four H-Tx (+) rats (copy number loss), and six of eight H-Tx (-) rats showed no copy number loss encompassing the *Ptpn20* gene (Fig. 1A, Additional file 4: Table S1). We further confirmed and quantified the alteration of copy numbers for the *Ptpn20* exon in twelve H-Tx (-) rats and six H-Tx (+) rats by real-time polymerase chain reaction (PCR). H-Tx (+) rats exhibited an approximately 2.4-fold decrease in exon 6 ($P < 0.01$) and 1.6-fold decrease in exon 7 ($P < 0.001$) in copy numbers of *Ptpn20* relative to H-Tx (-) rats (Fig. 1A). After this, we confirmed differential expression of *Ptpn20* mRNA in the brains of H-Tx (+) rats, H-Tx (-) rats, SD rats and Wistar rats by real-time PCR. H-Tx (+) rats showed almost half the amount of *Ptpn20* mRNA expression compared to other rat lineages and H-Tx (-) rats (Fig. 1B). Subsequently, we detected *Ptpn20* protein expression in H-Tx (-) and H-Tx (+) rats using immunoblot, which showed immunoreactivity to a 50-kDa *Ptpn20* protein to be approximately absent or lower in the choroid plexus (CP) of H-Tx (+) rats (Fig. 1C). Moreover, immunofluorescent staining (IF) also showed *Ptpn20* immunoreactivity in CP epithelial cells of H-Tx (-) and SD rats, while immunoreactivity was low in H-Tx (+) rats (Fig. 1D).

Analysis of *Ptpn20* expression in mice

To assess *Ptpn20* expression and distribution in C57BL/6J mice, we examined the expression of *Ptpn20* mRNA in different regions of the brain as well as several tissues (heart, lung, spleen, kidney, liver, and testis) from 4-week-old mice using real-time PCR. *Ptpn20* mRNA was expressed mainly in brain and testis. In the brain, *Ptpn20* mRNA was expressed in the CP, hippocampus, and cerebral cortex. *Ptpn20* mRNA expression levels were 2.73- and 1.92-fold higher in the CP than in the cerebral cortex and hippocampus, respectively. However, *Ptpn20* mRNA showed its highest expression in the testis, at 415-fold higher than in the CP. In contrast, no expression was detected in other tissues (Fig. 2A). These results were further validated in immunohistochemical staining of murine heart, lung, spleen, pancreas, liver, testis, and CP using *Ptpn20* antibody. The staining showed extremely strong immunoreactivity in the testis and CP epithelial cells, but no change in other tissues (Fig. 2B, Additional file 2: Fig. S2).

Generation of *Ptpn20*-knockout mice

To investigate whether deletion of *Ptpn20* represents a risk factor for hydrocephalus, we generated *Ptpn20*-knockout (*Ptpn20*^{-/-}) mice using CRISPR/Cas9 technology. We targeted and generated a sgRNA against exon 4 of the *Ptpn20* mouse gene. DNA sequencing results confirmed the targeted 104-bp deletion mutations in *Ptpn20*^{-/-} mice (Fig. 3A). For immunoblot analysis, *Ptpn20* protein was almost completely absent in the CP of *Ptpn20*^{-/-} mice (Fig. 3B). We then performed IF using anti-*Ptpn20* and anti-F-actin antibodies. *Ptpn20* was detected in the cytoplasm of CP epithelial cells in WT mice, but not in ependymal cells, and expression was completely abolished in *Ptpn20*^{-/-} mice. F-actin staining showed no obvious difference between WT and *Ptpn20*^{-/-} mice (Fig. 3C). Transmission electron microscopy (TEM) applied to detect substantial structural differences revealed no obvious differences between the CP epithelial cells of WT and *Ptpn20*^{-/-} mice (Fig. 3D).

***Ptpn20*^{-/-} mice develop communicating hydrocephalus**

Ptpn20^{-/-} mice seemed to have normal appearance and lifespan, because almost all lived to over 18 months. To elucidate the morphology of the brain and ventricles of *Ptpn20*^{-/-} mice, we analyzed brain slices from 8-week-old mice by hematoxylin and eosin (HE)-staining. Mean relative ventricle-to-brain ratio (VBR) was 0.11 ± 0.01 for WT mice and 0.14 for *Ptpn20*^{-/-} mice ($P < 0.01$). In *Ptpn20*^{-/-} mice, VBR exceeding the mean WT value by 2 standard deviations was defined as indicating hydrocephalus. Of these 29 *Ptpn20*^{-/-} mice, 16 mice met the criteria for hydrocephalus, and 13 mice did not develop hydrocephalus, while some of the hydrocephalic mice exhibited very mild ventriculomegaly (Fig. 4A). To establish whether an anatomical defect resulted in hydrocephalus, we injected Evans blue in the lateral ventricle of *Ptpn20*^{-/-} mice. Blue dye appeared in the aqueduct, the fourth ventricle and the atlantooccipital subarachnoid space in all cases, suggesting the entire CSF drainage pathway was patent (Fig. 4B).

Phosphorylation of NKCC1 is maintained in CP epithelial cells of *Ptpn20*^{-/-} mice

To further explore connections between the pathogenesis of hydrocephalus and CP in *Ptpn20*^{-/-} mice, we compared aquaporin 1 (AQP1), sodium-potassium adenosine triphosphatase (Na⁺/K⁺-ATPase), and Na-K-Cl cotransporter (NKCC1) expressions in the CP as proteins involved in the secretion or absorption of CSF. No significant differences in the mRNA expressions of AQP1, Na⁺/K⁺-ATPase, or NKCC1 were detected in the CP by real-time PCR (Fig. 5A). We then used immunoblotting techniques to investigate the expression of phosphorylated NKCC1 (pNKCC1) in the CP, which correlates with the phosphorylation of Thr212/Thr217 in its N-terminal domain. *Ptpn20*^{-/-} mice showed differential increase in levels of pNKCC1 expression from 8 weeks until 72 weeks compared with WT (Fig. 5B, Additional file 3: Fig. S3A). Furthermore, consistent with our immunoblotting results, IF analysis of CP sections labeled with pNKCC1 antibody showed significantly increased expression of pNKCC1 in the apical membrane of CP epithelial cells in *Ptpn20*^{-/-} mice, while no significant differences were seen there for unphosphorylated NKCC1, AQP1 or Na⁺/K⁺-ATPase compared with the WT (Fig. 5C).

Discussion

This study identified copy number loss of *Ptpn20* in the brain of H-Tx (+) rats. *Ptpn20* was enriched in the CP of non-hydrocephalic rats, but significantly decreased in the CP of H-Tx (+) rats. We then generated *Ptpn20*-deficient mice to investigate whether the deletion of *Ptpn20* is a risk for hydrocephalus. *Ptpn20*^{-/-} mice do not exhibit the characteristics of congenital hydrocephalus observed in H-Tx rats after birth. However, further analysis in adult *Ptpn20*^{-/-} mice revealed ventriculomegaly in more than half of these mice without significant blockage of CSF circulatory pathways, thus indicating that *Ptpn20*^{-/-} mice had developed communicating hydrocephalus. Since hydrocephalus is not associated with stenosis of the cerebral aqueduct, we further investigated the CP, which is mainly affected by *Ptpn20* deletion. Previous studies have shown that structural or functional abnormalities of CP may affect CSF production and thus lead to the development of hydrocephalus [25-27]. To evaluate possible CP abnormalities, we analyzed the ultrastructure of the CPs of the lateral and third ventricles in *Ptpn20*^{-/-} mice using TEM. A normal

appearance of the CP epithelium and intact junctions between cells suggest that passive diffusion of molecules from the CP vasculature into the CSF is unlikely. However, in analyzing the channels and transporters involved in ion and water transport for CP epithelial cells, we found that expression of pNKCC1 protein was mainly at the apical surface of CP epithelial cells and was significantly increased in about half of *Ptpn20*^{-/-} mice as compared with WT mice. This result may provide useful insights into the pathogenesis of hydrocephalus, and the individual differences in the degree of pNKCC1 expression seem to explain why only half of the knockout mice developed hydrocephalus.

NKCC1 is located on the basolateral membrane and is involved in active transportation of Na⁺, K⁺, and Cl⁻, which play important roles in fluid absorption and secretion in most epithelial tissues. However, NKCC1 in the brain is highly expressed in the apical membrane of CP epithelial cells [28]. Several studies have shown that inhibition of NKCC1 by bumetanide leads to decreased CSF production in the CP [29-32]. Ex vivo and in vivo studies have shown that NKCC1 contributes approximately half of the CSF production that is independent of the osmotic gradient [31]. In addition, previous studies have shown that increased NKCC1 activity is associated with direct phosphorylation of NKCC1 [33], suggesting that enhanced or continued NKCC1 phosphorylation may result in greater CSF production by the CP. A previous study showed that in a rat model of posthemorrhagic hydrocephalus, inflammation-induced phosphorylation of NKCC1 caused hypersecretion of CSF [34].

Ptpn20 is a member of the PTPs family, which, together with protein tyrosine kinases, is responsible for regulating the phosphorylation state of intracellular protein [35]. The function of *Ptpn20* is not yet completely understood. Limited studies have shown that *Ptpn20* is expressed in a variety of cell lines, showing a dynamic subcellular distribution in response to various extracellular stimuli targeting sites of actin polymerization [36]. Previous studies have shown that inhibition of actin polymerization with cytochrome D increases NKCC1 activity in colonic cells [37, 38]. However, our results did not show obvious differences in F-actin staining (Fig. 3C), suggesting that *Ptpn20* correlates with actin, but has no significant effects on actin polymerization or depolymerization.

On the other hand, NKCC1 activity is known to be regulated by phosphorylation of its specific Serine/Threonine residues [39]. Although tyrosine residues have not been identified in NKCC1, NKCC1 can be tyrosine-phosphorylated by tyrosine kinase and inhibition of tyrosine kinase decreased NKCC1 activity by around 50% [40, 41]. This finding suggests that NKCC1 phosphorylation is regulated by a pathway that can be activated by tyrosine kinases. This also suggests that NKCC1 might be dephosphorylated by the tyrosine phosphatase encoded by *Ptpn20*. Deletion of *Ptpn20* may thus cause NKCC1 to fail to dephosphorylate and so persistently remain in the phosphorylated state, and our results showing increased expression of pNKCC1 in *Ptpn20*^{-/-} mice from 8 to 72 weeks support this concept. This change would result in a continuous excess of CSF entering the ventricular system. In humans, CSF hypersecretion secondary to CP hyperplasia or CP papilloma disturbs the homeostasis of CSF production and absorption in the brain, leading to hydrocephalus [42, 43], and higher secretion rates correlate with more severe hydrocephalus [44]. We therefore consider that CSF hyperproduction may be a direct cause of hydrocephalus in this study. To further confirm this hypothesis, we also examined pNKCC1 expression

in H-Tx rats, and we found that pNKCC1 expression was significantly increased in the choroid plexus of H-Tx rats compared to SD rats (Additional file 3: Fig. S3B). This result suggests that increased expression of pNKCC1 due to *Ptpn20* deficiency is a potential factor contributing to hydrocephalus in both rats and mice.

However, *Ptpn20*^{-/-} mice did not exhibit severe hydrocephalus after birth like H-Tx rats, and we hypothesize that this may be because *Ptpn20*^{-/-} mice did not develop aqueductal stenosis during development or that the overproduction of CSF caused by NKCC1 in the genetic background of C57BL/6J was insufficient to cause severe hydrocephalus. Aqueductal stenosis is associated with abnormal development and dysfunction of the subcommissural organ (SCO) in H-Tx rats. The SCO is a secretory gland of epithelial cells dorsal to the aqueduct of the brain, and in H-Tx rats with congenital hydrocephalus, immunoreactivity of the SCO and glycoproteins of midbrain epithelial cells is decreased starting from embryonic day 16, before ventricular enlargement. Abnormal secretion of glycoprotein is known to interfere with the formation of Reissner's fiber, obstructing the cerebral aqueduct and leading to ventricular enlargement on embryonic day 17 [45]. This finding is consistent with other animal models regarding the link between SCO function and hydrocephalus [46]. Although the gene for hydrocephalus in H-Tx rats has not been identified, quantitative trait analysis suggests that the loci associated with the hydrocephalus phenotype are present on chromosomes 9, 10, 11, and 17 [24]. In contrast, the *Ptpn20* gene, located on chromosome 16, may not be involved in the developmental process of SCO.

Furthermore, in a study of L1-deficient mice, significantly enlarged ventricles were observed only in mutant mice backcrossed to the C57BL/6J genetic background, whereas the ventricular system appeared normal when the same mutant mouse strain was backcrossed to the 129 genetic background [47]. In addition, Cai et al. [19] found a lower than expected incidence of hydrocephalus and milder disease than in H-Tx rats when they cross-mated hydrocephalic H-Tx rats, and suggested that this result might be due to the effects of gene modifications in different genetic backgrounds. Similarly, the role of the *Ptpn20* gene may be enhanced in the genetic background of H-Tx rats and diminished in C57BL/6J mice. In addition, another study on L1 mutants showed that ventricular enlargement preceded the onset of aqueductal stenosis, and that massive enlargement of the ventricles caused deformation of the brain, which in turn compressed the aqueduct, leading to severe hydrocephalus [48]. Based on this hypothesis, we consider that although phosphorylation of NKCC1 may produce excess CSF, its production rate might be relatively mild and constant, and so may be insufficient to create an unbalanced pressure differential within the ventricular system that would result in brain deformation. As a result, only moderate hydrocephalus developed.

This study had several limitations. First, since accurately determining whether H-Tx rats at P18 have hydrocephalus based solely on appearance is difficult, hydrocephalic H-Tx rats may have been present among the current non-hydrocephalus samples, masking other genetic risk factors. Future studies will be needed, with larger sample sizes and improved sensitivity of the results, to identify other possible causative genes. Eventually, paired or multiple knockout models can be established to further clarify the molecular mechanisms underlying hydrocephalus. On the other hand, since reliable methods to

accurately measure CSF production remain lacking, it is not possible to test the hypothesis of CSF overproduction in *Ptpn20*^{-/-} mice. In addition, the lack of imaging tools makes the degree of ventricular dilatation impossible to determine directly from live animals. Isolated or dehydrated brain tissue may result in varying degrees of morphological and structural alteration of the ventricles, which may in turn have affected the accuracy of our results.

Conclusion

Our strategy of identifying potential pathogenic genes in hydrocephalic H-Tx rats and elucidating mechanisms in transgenic mouse models revealed the unexpected pathological relevance of hydrocephalus to *Ptpn20* deficiency. *Ptpn20* makes a substantial contribution to CSF production and provides a novel approach for diagnosing hydrocephalus. Furthermore, inhibition of the phosphorylation pathway of NKCC1 by protein tyrosine phosphatase may represent a therapeutic target for the management of hydrocephalus in the future.

Abbreviations

H-Tx: Hydrocephalus-Texas

H-Tx (-): Non-hydrocephalic H-Tx

H-Tx (+): Hydrocephalic H-Tx

CSF: Cerebrospinal fluid

SD: Sprague-Dawley

WT: Wild type

CGH: Comparative genomic hybridization array

PBS: Phosphate buffered saline

PCR: Polymerase chain reaction

CRISPR: Clustered regularly interspaced short palindromic repeats

sgRNA: Single guide RNA

CP: Choroid plexus

IF: Immunofluorescent staining

TEM: Transmission electron microscopy

HE: Hematoxylin and eosin

VBR: Ventricle-to-brain ratio

AQP1: aquaporin 1

Na⁺/K⁺-ATPase: Sodium-potassium adenosine triphosphatase

NKCC1: Na-K-Cl cotransporter

pNKCC1: phosphorylated NKCC1

Declarations

Ethics approval and consent to participate

All procedures involving animals were approved by the Ethics Review Committee for Animal Experimentation of the Juntendo University School of Medicine (rats: approval no. 288; mice: approval no. 1337) and followed the Principles of Laboratory Animal Care as outlined by the National Institutes of Health.

Consent for publication

Not applicable.

Availability of data and materials

Data are available from the corresponding author with reasonable request.

Competing interests

The authors declare that they have no competing interests.

Funding

This study was financially supported by the Juntendo Research Branding Project and the Japan Society for the Promotion of Science under Grants-in-Aid for Scientific Research (grant numbers 18H02916, 20K09355, 20K09398).

Authors' contributions

MM, MN and HBX designed the experiments; HBX performed immunohistochemistry, HE-staining and dye injection, analyzed all of the data and wrote the manuscript; IO performed CGH array, real-time PCR, immunoblotting and immunofluorescence, KM performed TEM imaging; KK provided English correction;

EN and NT generated knockout mice; and MM, MN, CA, CK, KS, HA and AK were responsible for critical review.

Acknowledgements

We gratefully acknowledge the contributions of the Laboratory of Morphology and Image Analysis, Laboratory of Biomedical Research Resources, Laboratory of Proteomics and Biomolecular Science, Laboratory of Molecular and Biochemical Research, Biomedical Research Core Facilities, Graduate School Research Program of Juntendo University, Juntendo University Research Institute for Diseases of Old Age and Juntendo University Graduate School of Medicine for their technical assistance.

References

1. Casey AT, Kimmings EJ, Kleinlugtebeld AD, Taylor WA, Harkness WF, Hayward RD. The long-term outlook for hydrocephalus in childhood. A ten-year cohort study of 155 patients. *Pediatr Neurosurg.* 1997;27(2):63-70; doi: 10.1159/000121229.
2. Garton HJ. Cerebrospinal fluid diversion procedures. *J Neuroophthalmol.* 2004;24(2):146-55; doi: 10.1097/00041327-200406000-00010.
3. Lun MP, Monuki ES, Lehtinen MK. Development and functions of the choroid plexus-cerebrospinal fluid system. *Nat Rev Neurosci.* 2015;16(8):445-57; doi: 10.1038/nrn3921.
4. Al-Dosari MS, Al-Owain M, Tulbah M, Kurdi W, Adly N, Al-Hemidan A, et al. Mutation in MPDZ causes severe congenital hydrocephalus. *J Med Genet.* 2013;50(1):54-8; doi: 10.1136/jmedgenet-2012-101294.
5. Ekici AB, Hilfinger D, Jatzwauk M, Thiel CT, Wenzel D, Lorenz I, et al. Disturbed Wnt Signalling due to a Mutation in CCDC88C Causes an Autosomal Recessive Non-Syndromic Hydrocephalus with Medial Diverticulum. *Mol Syndromol.* 2010;1(3):99-112; doi: 10.1159/000319859.
6. Rosenthal A, Jouet M, Kenrick S. Aberrant splicing of neural cell adhesion molecule L1 mRNA in a family with X-linked hydrocephalus. *Nat Genet.* 1992;2(2):107-12; doi: 10.1038/ng1092-107.
7. Adle-Biassette H, Saugier-Veber P, Fallet-Bianco C, Delezoide AL, Razavi F, Drouot N, et al. Neuropathological review of 138 cases genetically tested for X-linked hydrocephalus: evidence for closely related clinical entities of unknown molecular bases. *Acta Neuropathol.* 2013;126(3):427-42; doi: 10.1007/s00401-013-1146-1.
8. Meiniel A. The secretory ependymal cells of the subcommissural organ: which role in hydrocephalus? *Int J Biochem Cell Biol.* 2007;39(3):463-8; doi: 10.1016/j.biocel.2006.10.021.
9. Merchant M, Evangelista M, Luoh SM, Frantz GD, Chalasani S, Carano RA, et al. Loss of the serine/threonine kinase fused results in postnatal growth defects and lethality due to progressive hydrocephalus. *Mol Cell Biol.* 2005;25(16):7054-68; doi: 10.1128/MCB.25.16.7054-7068.2005.
10. Zhang J, Williams MA, Rigamonti D. Genetics of human hydrocephalus. *J Neurol.* 2006;253(10):1255-66; doi: 10.1007/s00415-006-0245-5.

11. Sasaki S, Goto H, Nagano H, Furuya K, Omata Y, Kanazawa K, et al. Congenital hydrocephalus revealed in the inbred rat, LEW/Jms. *Neurosurgery*. 1983;13(5):548-54; doi: 10.1227/00006123-198311000-00011.
12. Clark FH. Linkage Studies of Brachyury (Short Tail) in the House Mouse. *Proc Natl Acad Sci U S A*. 1934;20(5):276-9; doi: 10.1073/pnas.20.5.276.
13. Hong HK, Chakravarti A, Takahashi JS. The gene for soluble N-ethylmaleimide sensitive factor attachment protein alpha is mutated in hydrocephaly with hop gait (hyh) mice. *Proc Natl Acad Sci U S A*. 2004;101(6):1748-53; doi: 10.1073/pnas.0308268100.
14. Cohen AR, Leifer DW, Zechel M, Flanigan DP, Lewin JS, Lust WD. Characterization of a model of hydrocephalus in transgenic mice. *J Neurosurg*. 1999;91(6):978-88; doi: 10.3171/jns.1999.91.6.0978.
15. Kohn DF, Chinookoswong N, Chou SM. A new model of congenital hydrocephalus in the rat. *Acta Neuropathol*. 1981;54(3):211-8; doi: 10.1007/BF00687744.
16. Jones HC, Lopman BA, Jones TW, Carter BJ, Depelteau JS, Morel L. The expression of inherited hydrocephalus in H-Tx rats. *Childs Nerv Syst*. 2000;16(9):578-84; doi: 10.1007/s003810000330.
17. Jones HC, Bucknall RM. Inherited prenatal hydrocephalus in the H-Tx rat: a morphological study. *Neuropathol Appl Neurobiol*. 1988;14(4):263-74; doi: 10.1111/j.1365-2990.1988.tb00887.x.
18. Oi S, Yamada H, Sato O, Matsumoto S. Experimental models of congenital hydrocephalus and comparable clinical problems in the fetal and neonatal periods. *Childs Nerv Syst*. 1996;12(6):292-302; doi: 10.1007/BF00301016.
19. Cai X, McGraw G, Pattisapu JV, von Kalm L, Willingham S, Socci D, et al. Hydrocephalus in the H-Tx rat: a monogenic disease? *Exp Neurol*. 2000;163(1):131-5; doi: 10.1006/exnr.1999.7301.
20. Jones HC, Carter BJ, Depelteau JS, Roman M, Morel L. Chromosomal linkage associated with disease severity in the hydrocephalic H-Tx rat. *Behav Genet*. 2001;31(1):101-11; doi: 10.1023/a:1010266110762.
21. Jones HC, Chen GF, Yehia BR, Carter BJ, Akins EJ, Wolpin LC. Single and multiple congenic strains for hydrocephalus in the H-Tx rat. *Mamm Genome*. 2005;16(4):251-61; doi: 10.1007/s00335-004-2390-4.
22. Jones HC, Depelteau JS, Carter BJ, Lopman BA, Morel L. Genome-wide linkage analysis of inherited hydrocephalus in the H-Tx rat. *Mamm Genome*. 2001;12(1):22-6; doi: 10.1007/s003350010226.
23. Jones HC, Harris NG, Rocca JR, Andersohn RW. Progressive tissue injury in infantile hydrocephalus and prevention/reversal with shunt treatment. *Neurol Res*. 2000;22(1):89-96; doi: 10.1080/01616412.2000.11741041.
24. Jones HC, Yehia B, Chen GF, Carter BJ. Genetic analysis of inherited hydrocephalus in a rat model. *Exp Neurol*. 2004;190(1):79-90; doi: 10.1016/j.expneurol.2004.06.019.
25. Banizs B, Pike MM, Millican CL, Ferguson WB, Komlosi P, Sheetz J, et al. Dysfunctional cilia lead to altered ependyma and choroid plexus function, and result in the formation of hydrocephalus. *Development*. 2005;132(23):5329-39; doi: 10.1242/dev.02153.

26. Liu B, Chen S, Johnson C, Helms JA. A ciliopathy with hydrocephalus, isolated craniosynostosis, hypertelorism, and clefting caused by deletion of Kif3a. *Reprod Toxicol.* 2014;48:88-97; doi: 10.1016/j.reprotox.2014.05.009.
27. Swiderski RE, Agassandian K, Ross JL, Bugge K, Cassell MD, Yeaman C. Structural defects in cilia of the choroid plexus, subfornical organ and ventricular ependyma are associated with ventriculomegaly. *Fluids Barriers CNS.* 2012;9(1):22; doi: 10.1186/2045-8118-9-22.
28. Brinker T, Stopa E, Morrison J, Klinge P. A new look at cerebrospinal fluid circulation. *Fluids Barriers CNS.* 2014;11:10; doi: 10.1186/2045-8118-11-10.
29. Javaheri S, Wagner KR. Bumetanide decreases canine cerebrospinal fluid production. In vivo evidence for NaCl cotransport in the central nervous system. *J Clin Invest.* 1993;92(5):2257-61; doi: 10.1172/JCI116829.
30. Keep RF, Xiang J, Betz AL. Potassium cotransport at the rat choroid plexus. *Am J Physiol.* 1994;267(6 Pt 1):C1616-22; doi: 10.1152/ajpcell.1994.267.6.C1616.
31. Steffensen AB, Oernbo EK, Stoica A, Gerkau NJ, Barbuskaite D, Tritsaris K, et al. Cotransporter-mediated water transport underlying cerebrospinal fluid formation. *Nat Commun.* 2018;9(1):2167; doi: 10.1038/s41467-018-04677-9.
32. Wright EM. Transport processes in the formation of the cerebrospinal fluid. *Rev Physiol Biochem Pharmacol.* 1978;83:3-34.
33. Zhang J, Cordshagen A, Medina I, Nothwang HG, Wisniewski JR, Winklhofer M, et al. Staurosporine and NEM mainly impair WNK-SPAK/OSR1 mediated phosphorylation of KCC2 and NKCC1. *PLoS One.* 2020;15(5):e0232967; doi: 10.1371/journal.pone.0232967.
34. Karimy JK, Zhang J, Kurland DB, Theriault BC, Duran D, Stokum JA, et al. Inflammation-dependent cerebrospinal fluid hypersecretion by the choroid plexus epithelium in posthemorrhagic hydrocephalus. *Nat Med.* 2017;23(8):997-1003; doi: 10.1038/nm.4361.
35. Lee H, Yi JS, Lawan A, Min K, Bennett AM. Mining the function of protein tyrosine phosphatases in health and disease. *Semin Cell Dev Biol.* 2015;37:66-72; doi: 10.1016/j.semcd.2014.09.021.
36. Fodero-Tavoletti MT, Hardy MP, Cornell B, Katsis F, Sadek CM, Mitchell CA, et al. Protein tyrosine phosphatase hPTPN20a is targeted to sites of actin polymerization. *Biochem J.* 2005;389(Pt 2):343-54; doi: 10.1042/BJ20041932.
37. Matthews JB, Smith JA, Hrnjez BJ. Effects of F-actin stabilization or disassembly on epithelial Cl⁻ secretion and Na-K-2Cl cotransport. *Am J Physiol.* 1997;272(1 Pt 1):C254-62; doi: 10.1152/ajpcell.1997.272.1.C254.
38. Matthews JB, Smith JA, Mun EC, Sicklick JK. Osmotic regulation of intestinal epithelial Na(+)-K(+)-Cl⁻ cotransport: role of Cl⁻ and F-actin. *Am J Physiol.* 1998;274(3):C697-706; doi: 10.1152/ajpcell.1998.274.3.C697.
39. Lytle C. Activation of the avian erythrocyte Na-K-Cl cotransport protein by cell shrinkage, cAMP, fluoride, and calyculin-A involves phosphorylation at common sites. *J Biol Chem.* 1997;272(24):15069-77; doi: 10.1074/jbc.272.24.15069.

40. Rasmussen LJ, Müller HS, Jørgensen B, Pedersen SF, Hoffmann EK. Osmotic shrinkage elicits FAK- and Src phosphorylation and Src-dependent NKCC1 activation in NIH3T3 cells. *Am J Physiol Cell Physiol.* 2015;308(2):C101-10; doi: 10.1152/ajpcell.00070.2014.
41. Selvaraj NG, Omi E, Gibori G, Rao MC. Janus kinase 2 (JAK2) regulates prolactin-mediated chloride transport in mouse mammary epithelial cells through tyrosine phosphorylation of Na⁺-K⁺-2Cl⁻ cotransporter. *Mol Endocrinol.* 2000;14(12):2054-65; doi: 10.1210/mend.14.12.0568.
42. Aziz AA, Coleman L, Morokoff A, Maixner W. Diffuse choroid plexus hyperplasia: an under-diagnosed cause of hydrocephalus in children? *Pediatr Radiol.* 2005;35(8):815-8; doi: 10.1007/s00247-005-1456-0.
43. Bettegowda C, Adogwa O, Mehta V, Chaichana KL, Weingart J, Carson BS, et al. Treatment of choroid plexus tumors: a 20-year single institutional experience. *J Neurosurg Pediatr.* 2012;10(5):398-405; doi: 10.3171/2012.8.PEDS12132.
44. Karimy JK, Duran D, Hu JK, Gavankar C, Gaillard JR, Bayri Y, et al. Cerebrospinal fluid hypersecretion in pediatric hydrocephalus. *Neurosurg Focus.* 2016;41(5):E10; doi: 10.3171/2016.8.FOCUS16278.
45. Somera KC, Jones HC. Reduced subcommissural organ glycoprotein immunoreactivity precedes aqueduct closure and ventricular dilatation in H-Tx rat hydrocephalus. *Cell Tissue Res.* 2004;315(3):361-73; doi: 10.1007/s00441-003-0843-9.
46. Pérez-Fígares JM, Jimenez AJ, Rodríguez EM. Subcommissural organ, cerebrospinal fluid circulation, and hydrocephalus. *Microsc Res Tech.* 2001;52(5):591-607; doi: 10.1002/1097-0029(20010301)52:5<591::AID-JEMT1043>3.0.CO;2-7.
47. Dahme M, Bartsch U, Martini R, Anliker B, Schachner M, Mantei N. Disruption of the mouse L1 gene leads to malformations of the nervous system. *Nat Genet.* 1997;17(3):346-9; doi: 10.1038/ng1197-346.
48. Rolf B, Kutsche M, Bartsch U. Severe hydrocephalus in L1-deficient mice. *Brain Res.* 2001;891(1-2):247-52; doi: 10.1016/s0006-8993(00)03219-4.

Figures

Figure 1

Identification and expression analysis of causative gene in H-Tx rats.

- A. The log2 ratio value is plotted on the x-axis. The y-axis represents the genomic position of probes. Genomic profiles indicate a 14-kbp focal loss in 16p16. Colored vertical lines indicate the number of samples with copy number loss and loss segments (brown square) with respect to *Ptpn20*.
- B. Real-time PCR of copy number in the *Ptpn20* exon of H-Tx (-) and H-Tx (+) rats at E18. exon 6: H-Tx (-) = 2.11 ± 0.78 , H-Tx (+) = 0.88 ± 0.47 ; exon 7: H-Tx (-) = 1.84 ± 0.37 , H-Tx (+) = 1.15 ± 0.25 (mean \pm standard

deviation, ** P < 0.01, *** P < 0.001; H-Tx (-) rats, n = 12; H-Tx (+) rats, n = 6).

C. Real-time PCR of RNAs from P1 rats in SD, Wistar, H-Tx (-) and H-Tx (+) groups to determine expression levels of *Ptpn20* in the brain. Data are normalized to β-actin and fold change is expressed relative to levels in the SD rat. SD = 1.00 ± 0.14; Wistar = 0.98 ± 0.15; H-Tx (-) = 1.20 ± 0.08; H-Tx (+) = 0.55 ± 0.19 (mean ± standard deviation, ** P<0.01, *** P<0.001; n = 5 rats per group).

D. Immunoblot analysis of *Ptpn20* protein from the CP of P1 H-Tx (-) and H-Tx (+) rats. The 50-kDa bands correspond to *Ptpn20* and nonspecific (n.s.) bands, respectively. *Ptpn20* protein shows low or approximately abolished expression in H-Tx (+) rats. Actin was used as a loading control (n = 5 rats per group).

E. Immunofluorescence images of the CP in P1 SD, H-Tx (-) and H-Tx (+) rats are immunolabeled with anti-*Ptpn20* (green) antibody and with DAPI (blue). *Ptpn20* appears enriched in the CP epithelium of SD and H-Tx (-) rats, with low expression in H-Tx (+) rats, Scale bar = 20 μm.

Figure 2

Ptpn20 expression in mice.

A. *Ptpn20* mRNA expression level in different brain regions and several tissues of 4-week-old C57BL/6J mice as analyzed by real-time PCR. Relative fold change was calculated using the $2^{-\Delta\Delta Ct}$ method. Data are normalized to β-actin and fold change is expressed relative to levels in the CP set at 1. Other values are as follows: hippocampus = 0.37; cortex = 0.52; testis = 415 (hippocampus = HIP, cerebellum = CB; n = 5 mice per group).

B. Representative photomicrographs of immunohistochemistry staining with anti-*Ptpn20* antibody in the CP of the third ventricle and testis from 4-week-old C57BL/6J mice. Scale bar = 50 μm; for zoom = 20 μm.

Figure 3

Generation of *Ptpn20*^{-/-} mice.

A. Schematic illustration of *Ptpn20* locus. *Ptpn20* gene was targeted at exon 4. The sgRNA sequence is underlined in yellow. The protospacer adjacent motif sequence is indicated in the red dotted box. Electropherograms of the 104-bp deletion mutations in exon 4 are indicated in the black dotted box (sgRNA = single guide RNA).

B. Expression levels of *Ptpn20* protein in CP were verified by immunoblotting. The 50-kDa bands correspond to *Ptpn20* and nonspecific bands. *Ptpn20* protein shows almost completely absence in the CP

of *Ptpn20*^{-/-} mice. Actin is used as the loading control (n = 5 mice per group).

C. Immunofluorescence of *Ptpn20* (green) and F-actin (red) in the CP of 8-week-old WT and *Ptpn20*^{-/-} mice. *Ptpn20* is almost completely absent in the CP of *Ptpn20*^{-/-} mice, while no significant difference is evident for F-actin compared to WT. Areas in square frames are magnified in the bottom panels. Top panels, scale bar = 50 µm; bottom panels, scale bar = 20 µm.

D. Representative transmission electron microscope images of longitudinal sections of lateral ventricle CP from 8-week-old WT and *Ptpn20*^{-/-} mice. No structural difference in CP is evident between WT and *Ptpn20*^{-/-} mice. Scale bar = 20 µm.

Figure 4

***Ptpn20*^{-/-} mice develop communicating hydrocephalus.**

A. Sagittal brain section showing acquisition sites of coronal brain slices. Representative micrograph of coronal and HE-stained brain sections showing distances measured for ventricle width (left, a; right, b) and brain width (c) in WT and *Ptpn20*^{-/-} mice. Ventricle-to-brain ratio (VBR) is calculated as the ratio of the sum of ventricular widths to brain width ((a+b) / c). *Ptpn20*^{-/-} mouse brain shows dilation of lateral ventricles. Histograms showing the VBR of WT and *Ptpn20*^{-/-} mice (mean ± standard deviation, Mann-Whitney U test, **P < 0.01; WT, n = 17; *Ptpn20*^{-/-} mice, n = 29).

B. Evans Blue injected into the lateral ventricles of *Ptpn20*^{-/-} mice at 8 weeks old shows slight enlargement of lateral ventricles with dye also seen in the fourth ventricle (n = 5; LV = lateral ventricle; 3V = third ventricle; Aq = aqueduct; 4V = fourth ventricle). Scale bar = 2 mm

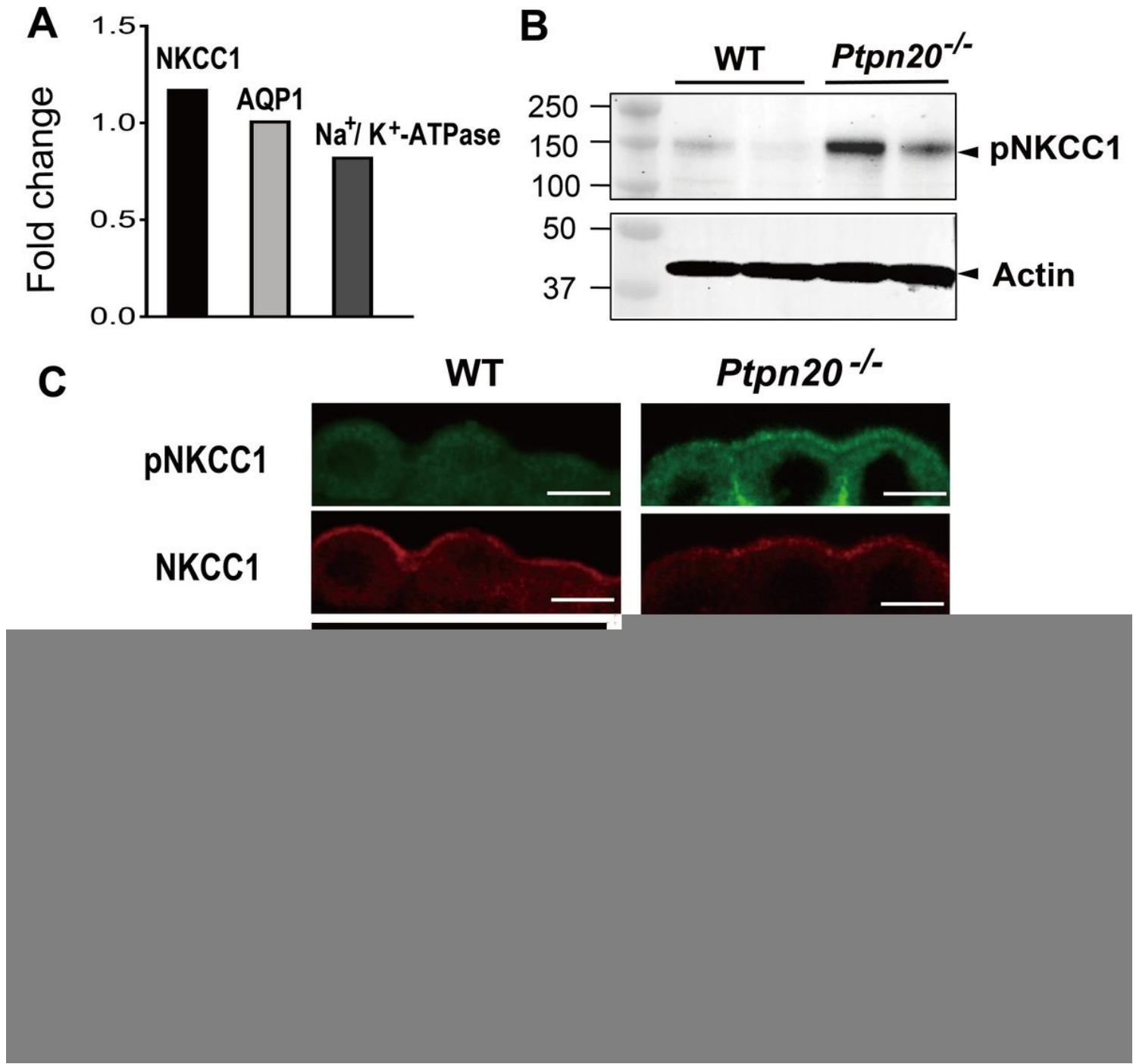


Figure 5

pNKCC1 expression is increased in the CP of *Ptpn20*^{-/-} mice.

A. Expressions of *Ptpn20*, water and ion transporters in the CP of *Ptpn20*^{-/-} mice as analyzed by real-time PCR. Relative fold change is calculated using the $2^{-\Delta\Delta Ct}$ method. Data are normalized to β -actin and fold change is expressed relative to the expression level of *Ptpn20* in the CP of WT mice set as 1. We did not find significant differences in expressions of NKCC1, AQP1 or Na^+/K^+ -ATPase in CP between 8-week-old WT and *Ptpn20*^{-/-} mice. Values are as follows: NKCC1 = 1.18; AQP1 = 1.01; ATP1a1 (Na^+/K^+ -ATPase) = 0.83 (n = 5 mice per group).

B. Immunoblotting of pNKCC1 protein expression in the CP of 8-week-old WT and *Ptpn20*^{-/-} mouse. Expression of pNKCC1 is higher in the CP of *Ptpn20*^{-/-} mice than in WT mice. Actin is used as the loading control (n = 5 mice per group).

C. Immunofluorescence of pNKCC1, NKCC1, AQP1 and Na⁺/K⁺-ATPase in 4-week-old WT and *Ptpn20*^{-/-} mice in the CP of the lateral ventricles and fourth ventricle are immunolabeled as shown. *Ptpn20*^{-/-} mice show stronger pNKCC1 expression in the cytoplasm and apical surface of CP epithelial cells than WT mice. No significant differences are seen in NKCC1, AQP1 or Na⁺/K⁺-ATPase between WT and *Ptpn20*^{-/-} mice. Scale bar = 10 μm.

Supplementary Files

This is a list of supplementary files associated with this preprint. Click to download.

- Additionalfile1.docx
- Additionalfile2.docx
- Additionalfile3.docx
- Additionalfile4.docx
- Additionalfile5.docx
- Additionalfile6.docx
- Additionalfile7.docx